# Elastin-like recombinamer-mediated hierarchical mineralization coatings on Zr-16Nb-xTi (x=4,16 wt.%) alloy surfaces improve biocompatibility

Renhao Xue<sup>a,c</sup>, Xinru Deng<sup>b</sup>, Xiaoning Xu<sup>a,c</sup>, Yueyan Tian<sup>a,c</sup>, Abshar Hasan<sup>d,e</sup>, Alvaro Mata<sup>d,e,f</sup>,
Ligang Zhang<sup>a,c\*</sup>, Libin Liu<sup>a,c\*</sup>

<sup>a.</sup> School of Materials Science and Engineering, Central South University, Changsha, Hunan

410083, PR China

b. School of Engineering and Materials Science, Queen Mary University of London, London,

E14NS, UK

<sup>c.</sup> State Key Laboratory of Powder Metallurgy, Central South University, Changsha, Hunan

410083, PR China

d. School of Pharmacy, University of Nottingham, Nottingham, NG7 2RD, UK

<sup>e.</sup> Biodiscovery Institute, University of Nottingham, Nottingham, NG7 2RD, UK

<sup>f.</sup> Department of Chemical & Environmental Engineering, University of Nottingham,

Nottingham, NG7 2RD, UK

\* Corresponding authors: Dr. Prof. Libin Liu; Dr. Prof. Ligang Zhang

E-mails: pdc@csu.edu.cn (Libin Liu); ligangzhang@csu.edu.cn (Ligang Zhang)

Telephone: 0086-731-88877732

### **Abstract**

The biocompatibility of biomedical materials is vital to their applicability and functionality. However, modifying surfaces for enhanced biocompatibility using traditional surface treatment techniques is challenging. We employed a mineralizing elastin-like recombinamer (ELR) self-assembling platform to mediate mineralization on Zr-16Nb-xTi (x=4,16 wt.%) alloy surfaces, resulting in the modification of surface morphology and bioactivity while improving the biocompatibility of the material. We modulated the level of nanocrystal organization by adjusting the cross-linker ratio. Nanoindentation tests revealed that the mineralized configuration had nonuniformity with respect to Young's modulus and hardness, with the center areas having higher values (5.626 $\pm$ 0.109 GPa and 0.264 $\pm$ 0.022 GPa) compared to the edges (4.282 $\pm$ 0.327 GPa and  $0.143\pm0.023$  GPa). The Scratch test results indicated high bonding strength  $(2.668 \pm 0.117 \text{ N})$  between the mineralized coating and the substrate. Mineralized Zr-16Nb-xTi (x=4,16 wt.%) alloys had higher viability compared to untreated alloys, which exhibited high cell viability (>100%) after 5 days and high alkaline phosphatase activity after 7 days. Cell proliferation assays indicated that MG 63 cells grew faster on mineralized surfaces than on untreated surfaces. Scanning electron microscopy imaging confirmed that the cells adhered and spread well on mineralized surfaces. Furthermore, hemocompatibility test results revealed that all mineralized samples were non-hemolytic. Our results demonstrate the viability of employing the ELR mineralizing platform to improve alloy biocompatibility.

**Keywords:** Elastin-like recombinamers, Self-assembly, Hierarchical mineralization, Biocompatibility, Zr alloys

### 1. Introduction

Metals and alloys are essential materials in biomedical applications because of their high strength and processability. Owing to continual advances in medical standards and the rapid evolution of medical equipment, metal- and alloy-based biomedical materials have been gaining attention for their improved performance criteria. The most critical demands for the characteristics of innovative biomedical materials are low Young's modulus, magnetic susceptibility, and biocompatibility [1].

Alloys, such as Ti-based materials, 316 L stainless steel, and Co-Cr-Mo alloys, are widely used in clinical settings, such as bone implants [2], owing to their remarkable mechanical properties and resistance to corrosion. However, Ti alloys (55–115 GPa) [3], 316 L stainless steel (200–210 GPa) [3,4], and Co-Cr alloys (210–253 GPa) [3,4] have much higher Young's modulus values than that of human bone (10–30 GPa) [5], resulting in a "stress shielding" effect that can lead to implant failure [6,7]. Furthermore, the high magnetic susceptibility of these alloys causes "artifacts" in a strong magnetic field (because high magnetic susceptibility disrupts the original magnetic field), leading to inaccurate diagnoses using magnetic-based imaging techniques. Although Ti alloys have lower magnetic susceptibility than most bio-alloys, they can cause image distortion during magnetic resonance imaging (MRI)-based diagnosis [8,9]. To address these immediate concerns, we previously designed a Zr-16Nb-xTi (x=0,4,8,12,16 wt.%) alloy with a lower Young's modulus (52 GPa) and magnetic susceptibility  $(1.92\times10^{-6} \text{ cm}^3/\text{g})$ , as well as high cytocompatibility. We tested the effect of this alloy on MG 63 cells, which remained highly viable (91–97%) after being cultured in the Zr-16Nb-xTi (x=0,4,8,12,16 wt.%) extraction media for 12 days [10]. Despite such advancements, there is an urgent need to enhance the biocompatibility and bioactivity of metallic implant materials to improve their effectiveness in various orthopedic applications, including stimulation of osseointegration and biomineralization during bone fracture healing [11].

The surface properties of metallic materials play important roles in regulating

implant biocompatibility, functionality, and safety [12,13,14,15,16,17,18,19]. Therefore, several surface treatment technologies have been developed to tune the surface texture of alloys [20,21,22,23]. Micro-arc oxidation is one of the most promising surface modification methods for generating porous microstructures and doping with bio-functional ions, such as calcium and phosphorus [24,25]. However, the process sometimes leads to uncontrollable pore formation, which reduces corrosion resistance and increases the propensity for mechanical failure [26]. Physical vapor deposition (PVD) techniques for coating bio-ceramics on Ti-alloy surfaces have also attracted attention. For example, Jeong et al. [27] prepared a hydroxyapatite (HA) coating on a nanotubular TiTaHf alloy using PVD methods to improve their cell adhesive capacity. However, this process has several disadvantages, including high cost, low efficiency, and poor crystallinity of the coating.

Surface treatments combined with protein-guided bioengineering technology are an attractive option for creating more bioactive alloys while offering a high level of tunability and the possibility of stimulating bone formation. Elastin-like recombinamers (ELRs) are genetically engineered protein-based polymers mainly composed of the repeating pentapeptide domain VPGXG, where X is any amino acid apart from proline [28]. These molecules can be easily functionalized with bioactive epitopes, such as RGDS and REDV, for cell adhesion, and the statherin-derived peptide sequence DDDEEKFLRRIGRFG to bind calcium phosphate [29,30]. We previously developed methods for modifying ELR conformations and assembled them into supramolecular ensembles capable of nucleating and organizing the development of fluorapatite nanocrystals [31]. We demonstrated that this matrix may be used as a coating [32], including mineralizing coatings for 3D-printed polymeric implants [33].

In this study, we extended the functionality of a previously developed platform to use ELRs (comprising a statherin-derived peptide sequence) as a self-assembling mineralizing coating for Zr-16Nb-4Ti and Zr-16Nb-16Ti alloy surfaces to enhance implant bioactivity. This method was hypothesized to increase the alloy biocompatibility of medical devices, such as dental implants and bone nails. The

mineralization microstructures and fluorapatite phase were examined, and alloy biocompatibility was evaluated in vitro using osteoblast-like MG 63 cells. We also evaluated the bioactivity and hemocompatibility differences between mineralized alloys and untreated alloys to demonstrate that our established method is practical and effective for enhancing alloy bioactivity.

### 2. Materials and Methods

### 2.1 Preparation of substrate materials

Zr-16Nb-4Ti and Zr-16Nb-16Ti alloys were prepared from pure Zr (≥99.99 wt.%), Nb (≥99.99 wt.%), and Ti (≥99.99 wt.%) using a non-consumable arc-melting furnace under an Ar atmosphere. The raw materials (Zr, Nb, and Ti) were provided by Beijing Jinyu Sunshine New Material Technology Co., Ltd. (China). The melting temperature was set at 3000 °C for sufficient mixing and reaction of the alloys in a molten state. Each alloy ingot was heated for 80 s, at which point all samples melted. The molten ingots were then directly cooled in copper melting pots maintained at 20 °C using running water. Each ingot was remelted six times by inversion to improve its chemical homogeneity. The ingots were placed in a vacuum tube furnace at 1000 °C for 2 h and quenched in ice water. Following that, the alloys were cut into wafers of 10 mm diameter and 1.5 mm thickness using electrical discharge machining. All wafers underwent mirror-polishing to generate a surface roughness of approximately 10 nm. The alloy composition determined by energy dispersive spectrometry (EDS) is shown in Supplementary Table 1.

#### 2.2 Elastin-like recombinamer membrane fabrication

The ELR coating(s) were fabricated on Zr-16Nb-4Ti and Zr-16Nb-16Ti discs using a previously reported procedure [31]. Briefly, 5 wt.% ELR molecules (Beijing Novin Biotechnology Co., Ltd., China) were dissolved in a solvent mixture containing anhydrous dimethylformamide (Sigma-Aldrich, UK) and dimethyl sulfoxide (Sigma-

Aldrich, UK) in a 9:1 ratio. Hexamethyl diisocyanate (HDI; Sigma-Aldrich, UK) cross-linker was then added at 25 °C under low humidity (<20%) inside a polymer glove box (TORUN Technology, China). Next, 10-mm Zr-16Nb-4Ti and Zr-16Nb-16Ti wafers were completely submerged in the solution and left to dry overnight.

### 2.3 Mineralization process

Hydroxyapatite powder (HAP, 2 mM, Sigma-Aldrich, UK) and sodium fluoride (NaF, 2 mM, Sigma-Aldrich, UK) were dissolved in deionized water under continuous stirring to obtain a mineralizing solution. To dissolve the HAP, 69% nitric acid (Aladdin, China) was added dropwise until the solution became clear. The pH of the solution was adjusted to 6.0 by adding a 30% ammonium hydroxide solution (Aladdin). For mineralization, ELR-coated Zr-16Nb-4Ti and Zr-16Nb-16Ti samples were incubated in a mineralizing solution at 37 °C for 8 days. Figure 1 illustrates the mineralization process.

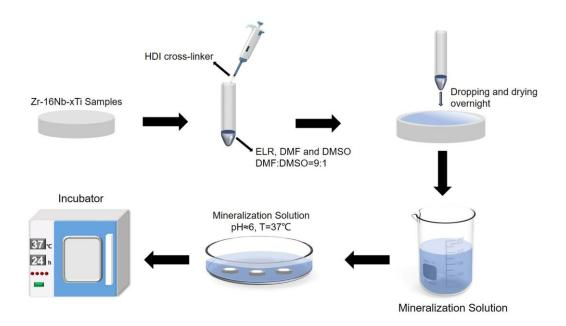


Figure 1. Schematic showing elastin-like recombinamer (ELR) protein membrane fabrication and mineralization process. DMSO, dimethyl sulfoxide; DMF, dimethyl formamide.

#### 2.4 Mineralization characterization

Mineralized Zr-16Nb-4Ti and Zr-16Nb-16Ti alloy surface topographies were observed using scanning electron microscopy (SEM, MIRA3 Tescan, Czech Republic) at a 10 kV accelerating voltage. The chemical composition of the mineralized structures was determined using EDS.

X-ray diffraction (XRD) using a Rigaku D/Max 2500 diffractometer with Cu-K $\alpha$  radiation (Rigaku, Tokyo, Japan) was used to identify the phase constitution of the mineralized Zr-16Nb-xTi (x=4,16 wt.%) samples, using accelerating voltage and current of 40 kV and 250 mA, respectively. The 2 $\theta$  values were recorded from 5 $^{\circ}$  to 70 $^{\circ}$  with a scanning speed of 1 $^{\circ}$ /min.

The Zr-16Nb-4Ti and Zr-16Nb-16Ti samples were analyzed before and after mineralization using a Fourier-transform infrared (FTIR) spectrometer (IS-50, Thermo-Fisher Scientific, Waltham, MA, USA), and 128 scans were acquired at a resolution of 4 cm<sup>-1</sup> in the wavenumber range of 4000 cm<sup>-1</sup> to 400 cm<sup>-1</sup>. The data were analyzed using OMNIC software (Version 8.2, Nicolet, Madison, USA), and the infrared spectrum curve was obtained using Origin software (2019 version, OriginLab, USA).

### 2.5 Mechanical properties test

An Anton Paar NHT2 indentation tester (Graz, Austria) was used to measure the elastic modulus and hardness of the mineralized structure based on the Oliver-Pharr method [34]. Loading and unloading rates were maintained at 40 mN/min, with a dwell time of 10 s. The Young's modulus and hardness of the mineralized structures were evaluated by taking the average of three points from the center and edge of each mineralized structure.

The bonding strength between the substrate and the coating is a measure of the coating stability. Therefore, two groups of mineralized samples were prepared; one of these was untreated, while the other was soaked in a simulated body fluid (SBF)

solution for 2 h. The bonding strength between the mineralized coating and the substrate for both groups was determined using a scratch tester (UMT-2, Bruker, Germany) with a conical diamond indenter (radius=200 µm). Three scratches of equal length (2 mm) were produced on the surface of each sample, the load force was increased from 0 N to 5 N at 2 N/min, and the variation of the friction force and acoustic signal of the load force were recorded from each scratch to determine the coating bonding strength.

### 2.6 Cytocompatibility test

The cytocompatibility of mineralized and untreated Zr-16Nb-xTi (x=4,16 wt.%) alloys was assessed using MG 63 human osteoblast-like cells. The MG 63 cell line was obtained from the Center for Medical Genetics and School of Life Science, Central South University. All cells were handled according to procedures approved by the Institutional Cell Care and Use Committee at Central South University.

The MG 63 cells were cultivated at 37 °C in minimum essential medium (MEM) containing 10% fetal bovine serum,  $100 \,\mu\text{g/mL}$  streptomycin, and  $100 \,\mu\text{g/mL}$  penicillin in a cell incubator in a humidified atmosphere of 5% CO<sub>2</sub>. The medium was changed every 3 days throughout the cell experiments.

Cell viability was indirectly assessed based on ISO 10993-12:2007 [35]. The cell culture medium served as a negative control, while untreated and mineralized Zr-16Nb-xTi (x=4,16 wt.%) alloys served as the reference groups. Minimum essential medium containing 10% dimethyl sulfoxide (DMSO) served as a positive control. The cells were initially seeded in 96-well plates at a density of  $4 \times 10^3$  cells per 100  $\mu$ L of medium, and they were then cultured for 24 h to enable cell attachment. The culture media was then substituted with the sample extracts and incubated for 1, 3, or 5 days. After cultivation, 10  $\mu$ L of 3-(4,5-dimethylthiazol-2-yl)-2,5-diphenyltetrazolium bromide (MTT, 5 mg/mL) [36] was added to each well, and the plates were incubated for 4 h in a dark environment. Subsequently, 100  $\mu$ L of formazan solubilization solution (10%)

sodium dodecyl sulfate in 0.01 M HCl) was added to each well. The spectrophotometric absorbance of the product in each well was measured using a microplate reader (Bio-Tek, Thermo Fisher Scientific, Waltham, MA, USA) at 570 nm, with a reference wavelength of 630 nm. The MG 63 cells were cultivated in the specimen-derived extraction media for 7 days at a density of  $4 \times 10^3$  cells per  $100~\mu L$  of the medium to assess alkaline phosphatase (ALP) activity [36]. The culture medium was removed, and  $100~\mu L$  of 1% Triton X-100 was added to acquire the cell lysates. The ability of ALP to hydrolyze phenyl-phosphate to phenol and phosphate at pH 10 was measured. ALP activity was proportional to absorbance. The reaction was conducted for 15 min at a temperature of 37 °C. The reaction product's absorbance at 545 nm was measured using a microplate reader (Bio-Tek). ALP activity was taken as the percentage of the negative control.

To observe the adhesion of MG 63 cells after different culturing periods, the specimens were fixed with 4% paraformaldehyde (PFA) for 30 min, stained with 4,6-diamidino-2-phenylindole (DAPI) for 10 min, and rinsed with PBS. Then, images of fluorescently stained cells were captured under an inverted fluorescence microscope. To further observe the adhesion and spread of MG 63 cells on the surfaces of mineralized samples, the experimental specimens were fixed with 2.5% glutaraldehyde at 4 °C for 12 h after 1 and 3 days of culturing and then dehydrated in different concentrations of ethanol (30%, 50%, 70%, 80%, 90%, and 100%) for 10 min. Differences in cell morphologies were visualized using SEM.

# 2.7 Hemocompatibility test

# 2.7.1 Hemolysis rate test

Anticoagulant human blood was mixed with 0.9% normal saline at a volume ratio of 4:5 to achieve a blood dilution. The samples were immersed in 10 mL normal saline and incubated in a water bath at 37 °C for 30 min. Then, 0.2 mL of diluted blood was added, and the centrifuge tube was gently shaken and incubated in a water bath for

60 min. The liquid in the tube was centrifuged at 1000 r/min for 5 min, and the supernatant liquid was transferred to a clean 12-well plate. The absorbance (OD) of the supernatant liquid of each well was measured using a UW spectrophotometer (Thermo Fisher Scientific) at 545 nm. The positive control group was composed of 10 mL of normal saline and 0.2 mL of diluted blood, while the negative control group was composed of 10 mL of distilled water and 0.2 mL of diluted blood. Each sample was measured three times to obtain the average value. The hemolysis rate (%) was calculated according to the following formula (1):

Hemolysis rate=
$$(OD_T - OD_{NC})/(OD_{PC} - OD_{NC}) \times 100\%$$
, (1)

where  $OD_T$  is the absorbance of the test sample,  $OD_{NC}$  is the absorbance of the negative control group, and  $OD_{PC}$  is the absorbance of the positive control group.

#### 2.7.2 Platelet adhesion test

Platelet-rich plasma was obtained from anticoagulated human blood centrifuged at a speed of 1000 r/min for 10 min. The test samples were immersed in platelet-rich plasma at a temperature of 37 °C for 1 h, followed by rinsing with normal saline for 2 min. After that, the sample was immobilized in a 2.5% glutaraldehyde solution for 12 h at 25 °C. The samples were then dehydrated by adding gradient alcohol (30%, 50%, 70%, 80%, 90%, and 100%) at intervals of 10 min. The sample surfaces were sprayed with gold after drying, and platelet adhesion on these surfaces was observed via SEM (MIRA3 Tescan, Czech Republic).

### 2.8 Statistical analysis

SPSS software (Version 18.0, IBM, Chicago, USA) was used for the statistical analysis. One-way analysis of variance (ANOVA), followed by post hoc Tukey's test, was used to analyze differences among the groups. Statistical significance was set at p<0.05 and p<0.01.

### 3. Results and Discussion

## 3.1 The rationale of the study design

The enhanced biocompatibility and bioactivity of implant materials are crucial for their application. We applied the ELR self-assembly method inspired by Elsharkawy and Deng et al. [31,32] to fabricate mineralized structures. We used the technique to modify Zr-16Nb-4Ti and Zr-16Nb-16Ti alloy surfaces with different ELR:HDI ratios to identify a suitable ELR:HDI ratio and obtain ideal mineralized structures. We conducted an in vitro biocompatibility test to examine the ability of the modified alloys to facilitate MG 63 cell adhesion and spread, encourage proliferation and differentiation, and simulate the interaction between the implant alloys and MG 63 cells. We compared them with untreated alloys and verified that this method improved alloy biocompatibility. We hypothesized that as a result of mineralizing the Zr-16Nb-4Ti and Zr-16Nb-16Ti alloys through ELR surface modification, the morphology of the fluorapatite (FAp) hierarchical structure would promote MG 63 cell adhesion, as these mineralization structures offer more contact areas for cells, and we proposed that the improved biocompatibility could affect the growth and differentiation of MG 63 cells.

# 3.2 Characterization of the ELR membrane mineralization nucleation point

Multiple mineralization nucleation points, called ELR spherulites, were detected within the ELR membrane after cross-linking with HDI. Spherulites offer appropriate positions to absorb calcium ions and promote mineralization crystal growth. Based on the study by Elsharkawy et al. [31], the ELR matrix can be measured using a polarized light microscope. We utilized this method to identify the ELR matrix on processed Zr-16Nb-xTi (x=4,16 wt.%) alloys. As shown in Figure 2a-c, the number of ELR spherulites increased as the ELR:HDI ratio increased, with the spherulites becoming more regular, approaching a "Maltese-like" shape. Multiple ELR spherulites were

observed in the ELR membranes on the alloy surfaces, showing that these samples could undergo mineralization.

# 3.3 FTIR- and XRD-based characterization of mineralized Zr-16Nb-xTi (x=4,16 wt.%) alloys

The presence of fluorapatite (Ca<sub>5</sub>(PO<sub>4</sub>)<sub>3</sub>F, FAp) is the key factor when judging the success of ELR mineralization. Thus, we used an FTIR spectrometer and an XRD diffractometer to detect the fluorapatite phase and relevant mineralization functional groups. Figure 2d illustrates mineralized Zr-16Nb-xTi (x=4,16 wt.%) alloy XRD patterns that correlate with fluorapatite phase peaks. Figure 2e displays the FTIR spectra of Zr-16Nb-xTi (x=4,16 wt.%) alloys before and after mineralization and confirms the chemical composition of the mineralized samples by showing the fluorapatite structure formation following mineralization.

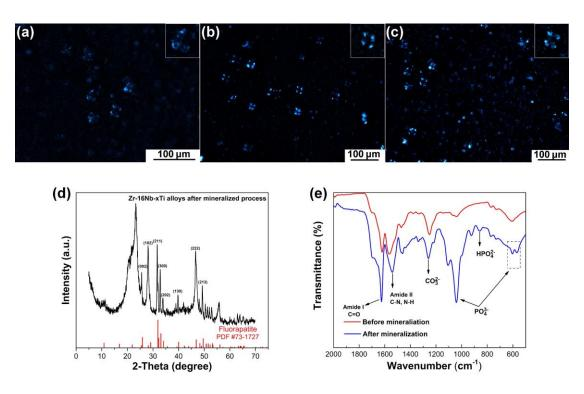


Figure 2. ELR spherulites and characterization of mineralized coatings. (a-c) Polarized light microscopy images confirm the presence of the ELR matrix within ELR membranes from Zr-16Nb-xTi (x=4,16 wt.%) alloy surfaces. (a) ELR:HDI=1:6. (b) ELR:HDI=1:12. (c) ELR: HDI=1:30. (d)

X-ray diffraction patterns of mineralized Zr-16Nb-xTi (x=4,16 wt.%) alloys, with reference patterns of standard fluorapatite phase. (e) Fourier-transform infrared spectroscopy analysis of the chemical characterization of mineralized Zr-16Nb-xTi (x=4,16 wt.%) samples and Zr-16Nb-xTi (x=4,16 wt.%) samples, including the ELR membrane. The red curve represents the main peaks corresponding to Amide I (C=O), Amide II (C-N, N-H), and CO<sub>3</sub><sup>2-</sup> functional groups, while the blue curve represents PO<sub>4</sub><sup>3-</sup> and HPO<sub>4</sub><sup>2-</sup> functional groups originating from fluorapatite.

# 3.4 Mineralization microstructures generated using different ELR:HDI ratios

Elsharkawy et al. [31] reported that the mineralized microstructure could be modified using different ELR:HDI ratios. Based on their research, we used three ELR:HDI ratios (1:6, 1:12, and 1:30) to explore different mineralized microstructures. The thickness and morphology of the mineralized coating on the longitudinal section are shown in Supplementary Figure 1.

Figure 3a-c illustrates the mineralized coating microstructure under a ratio of ELR: HDI=1:6. The mineralized structure is mostly disc-shaped and presents a low degree of divergence from the center to the outside. The diameter of the disc is approximately 18 µm. However, when the ELR:HDI ratio was increased to 1:12, the density of the mineralized microstructure increased (Figure 3d-f), and the microstructure had high divergence, more detail, and a dendritic shape growing divergently from the central nucleation point, displaying a hierarchical structure. Interestingly, although it shows the same ELR:HDI ratio, Figure 3g-i presents a different structure, with an obvious orientation not radiating from the center to the surroundings but growing in one direction, similar to the microstructure of human tooth enamel [31]. Moreover, the hierarchical structure identified here is more serried than human tooth enamel, showing a higher degree of integration, a property that was also reported in the microscopic structure of tooth enamel in a study by Ruan [37], which showed the microstructure of human tooth enamel from the nanometer to millimeter levels. Ruan reported that the

mineralized hierarchical structure is not only dense, but it also has obvious oriented growth characteristics at the nanometer level, similar to the mineralized structure shown here in Figure 3g-i. Ruan pointed out that at the nanometer scale, mature tooth enamel consists of highly ordered HA crystallites, with the thickness of the crystallites gradually increasing outwards from the cementum-enamel boundary. The appearance of these structures, called rods (prismatic) and inter-rods (enamel stroma), is more complex at the micron level. These structures are viewed as the basic building blocks of mammalian tooth enamel. The boundary between the rod and the enamel is a narrow space that contains organic material called a "rod sheath." Figure 3d-f displays analogous structures. At higher magnification, the rods and interrod enamel assemble into a unique structural pattern with different arrangements in the thickness of the glaze layer. The mineralized coating obtained using ELR proteins simulates the microstructure of human tooth enamel and is expected to greatly improve the biological activity and biocompatibility of the modified materials.

The mineralized microstructure changed once again when the ELR:HDI ratio was increased to 1:30. As shown in Figure 3j-l, the dendritic structure of the hierarchical mineralized structure was thicker (0.36  $\mu$ m) than that of the structure obtained using a 1:12 ratio (0.23  $\mu$ m). The microscopic organization of the dendritic structure was also more delicate, with a tiny hierarchical structure inside the thick dendritic structure. This structure had a greater degree of surface relief when viewed at the micron scale.

Therefore, we concluded that it is possible to modulate mineralization microstructures by adjusting the ELR:HDI ratio when designing a mineralized coating to simulate different microstructures in the human body. The mineralized structure obtained using an ELR:HDI ratio of 1:12 was more similar to human dental enamel, so we selected it for further study and performed additional, comprehensive characterization and evaluation of its properties as a bioactive material.

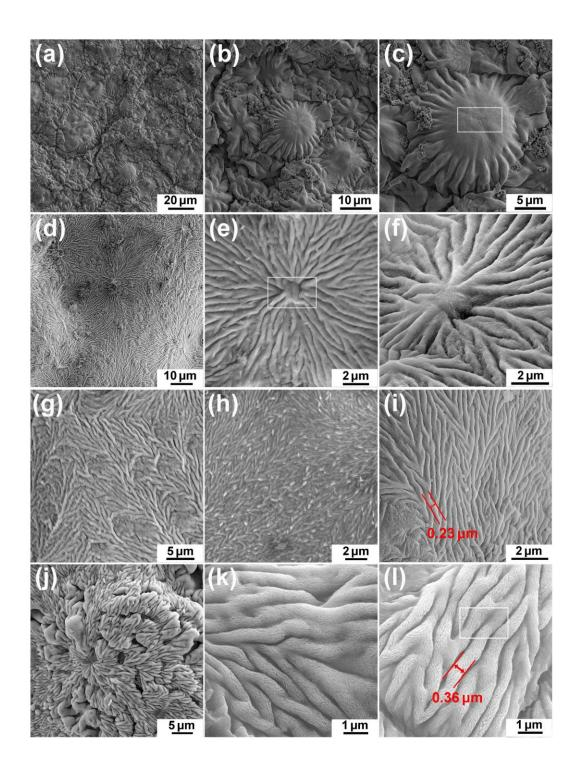


Figure 3. Scanning electron microscopy (SEM) images of mineralized structures on the surfaces of Zr-16Nb-xTi (x=4,16 wt.%) alloys following mineralization with different ratios of elastin-like recombinamer (ELR) and hexamethyl diisocyanate (HDI) cross-linkers. The white box represents the energy dispersive spectrometry (EDS) scanning area. (a-c) The mineralized texture of structures with an ELR:HDI cross-linker ratio of 1:6. (d-f) The radial mineralized structure with an ELR:HDI ratio of 1:12. (j-

#### 1) The mineralized structure with an ELR:HDI ratio of 1:30.

To further determine the chemical element composition of the mineralized structures, we performed SEM-EDS on representative mineralized structures generated using different ratios of ELR protein and HDI cross-linker (1:6, 1:12, and 1:30) and identified the elements and their relative contents, as shown in Figure 3 c, e, and I. Table 1 shows the presence of calcium, fluoride, and phosphorus, indicating the existence of fluorapatite crystals, which is consistent with the XRD and FTIR characterization. Bentov et al. [38] reported that F/Ca and P/Ca values were an important indicator of the presence of fluorapatite crystals, which have F/Ca and P/Ca values of approximately 0.2 and 0.6, respectively. Table 2 shows the F/Ca and P/Ca values of the different mineralized structures. The ELR:HDI = 1:6 structure had the largest F/Ca value (0.347), while the ELR:HDI = 1:30 structure had the smallest value (0.308). For P/Ca, the ELR:HDI = 1:12 structure had the largest value (0.630), while the remaining structures had similar values of 0.564 and 0.530. Overall, the different mineralized structures had the expected range of F/Ca and P/Ca values, verifying the presence of fluorapatite crystals.

Table 1. SEM-EDS results of mineralized structures on the surfaces of Zr-16Nb-xTi (x=4,16 wt.%) alloys with different ELR and HDI cross-linker ratios after mineralization

ELR:HDI	Concentration	С	О	F	P	Ca	Total
1:6	Wt.%	10.21	36.03	5.53	14.66	33.57	100
	At.%	18.07	47.87	6.19	10.06	17.81	100
1:12	Wt.%	9.12	30.71	5.42	17.93	36.82	100
	At.%	17.00	43.02	6.40	12.98	20.60	100
1:30	Wt.%	11.81	33.27	5.16	14.47	35.29	100
	At.%	21.00	44.41	5.80	9.98	18.80	100

Table 2. F/Ca and P/Ca ratio of mineralized structures on the surfaces of Zr-16Nb-xTi (x=4,16 wt.%) alloys with ELR and HDI cross-linker ratios of 1:6, 1:12, and 1:30 after mineralization

ELR:HDI	F/Ca (a.t%)	P/Ca (a.t%)
1:6	0.347	0.564
1:12	0.311	0.630
1:30	0.308	0.530

# 3.5 Mechanical properties of mineralized structures composed of a 1:12 ratio of ELR:HDI

Mechanical properties are vital to the performance of biomedical materials. We used nanoindentation to measure the mechanical performance based on the Young's modulus and hardness of the mineralized structure, and we employed a scratch tester to determine the bonding strength of the mineralized coating. Figure 4a shows the displacement-load curves of the samples. The curves of the central and surrounding parts have a certain offset, indicating that the mechanical properties of the two regions are different. Figure 4b shows the Young's modulus and hardness of the two regions. Figure 4c displays the bonding strength of the untreated samples and those soaked in SBF solution.

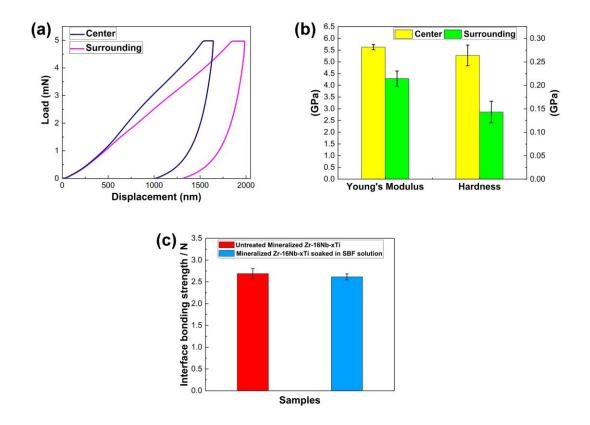


Figure 4. Nanoindentation analysis of mineralization structure with an ELR:HDI ratio of 1:12. (a) Displacement-load curves. (b) Young's modulus and hardness of the structure. (c) Bonding strength between mineralized coating and substrate under different conditions.

The Young's modulus and hardness of the central part  $(5.626\pm0.109 \text{ GPa})$  and  $0.264\pm0.022 \text{ GPa})$  were higher than those of the edges  $(4.282\pm0.327 \text{ GPa})$  and  $0.143\pm0.023 \text{ GPa})$ . These data are similar to those obtained by Elsharkawy et al.  $(8.2\pm1.4 \text{ GPa}, 0.6\pm0.1 \text{ GPa}, \text{center part})$  [31], although they are lower than the mechanical properties of bone  $(22.5\pm1.3 \text{ GPa}, 0.5\pm0.2 \text{ GPa})$  [39] and dental enamel  $(19.4\pm1.7 \text{ GPa}, 0.5\pm0.02 \text{ GPa})$  [40]. However, Elsharkawy et al. [31] verified the possibility of modulating the mechanical properties of mineralized structures by adjusting the ELR:HDI ratio. They showed that a higher Young's modulus and hardness  $(33\pm20.1 \text{ GPa})$  and  $1.08\pm0.81 \text{ GPa})$  were observed when the ELR:HDI ratio was lower, which has implications for the regulation of the mechanical properties of mineralized structures.

The bonding forces of untreated mineralized samples and samples soaked in SBF solution for 2 h were  $2.668 \pm 0.117$  N and  $2.615 \pm 0.067$  N, respectively, indicating that the mineralized coating was able to maintain relatively high stability in the SBF environment. Moreover, our mineralized coating had higher bonding strength compared with the protein-modulated calcium phosphate coating  $(0.33 \text{ N} \times 1.75 \text{ N})$  reported by Liu et al. [41] and the HA coating  $(0.04 \text{ N} \times 0.135 \text{ N})$  reported by Ohtsu et al. [42], indicating a strong connection between the mineralized coating and substrate.

# 3.6 Biocompatibility test of mineralized structures with an ELR:HDI ratio of 1:12

### 3.6.1 Adhesion of MG 63 cells

Clinical experiments have shown that the strength of biological bonding with the host is the main factor in determining an implant's life. The first step in the formation of biological bonding is the adhesion and spreading of osteoblasts on the surface of the implant. Therefore, the ability of osteoblasts to adhere to the material surface is a crucial indicator when evaluating its biocompatibility [43,44]. Figure 5a-1 shows fluorescence images of MG 63 cells cultured on untreated and mineralized Zr-16Nb-xTi (x=4,16 wt.%) alloy surfaces for 1, 4, and 24 h. The cells were stained with DAPI dihydrochloride after cultivation. The blue dots represent the nuclei. The number of MG 63 cells on the surfaces of mineralized Zr-16Nb-xTi (x=4,16 wt.%) alloys was much higher than on the surfaces of untreated Zr-16Nb-xTi (x=4,16 wt.%) alloys after 1 h (Figure 5a-d), and most of the cells were located on the edges of the mineralized structure, indicating that the mineralized structure facilitated the adhesion of MG 63 cells. The difference between the untreated and mineralized samples increased even more after 4 h of cultivation. The number of MG 63 cells on the surface of the mineralized alloy was much higher than on the surface of the untreated alloy. Moreover, since the surface of the mineralized sample was not entirely flat but had a degree of undulation, MG 63 cells adhered to different levels of the mineralized structure. The

fuzzy light blue spots are MG 63 cells, which adhered to lower sections of the structure. The number of MG 63 cells on the surface of the untreated Zr-16Nb-xTi (x=4,16 wt.%) alloy also significantly increased after 24 h. However, it remained lower than the number of cells adhering to the mineralized alloy.

To count the number of MG 63 cells on different surfaces, we selected three adjacent areas on the same sample and calculated the average value. The MG 63 cell numbers are shown in Figure 5m. The number of MG 63 cells on the surfaces of Zr-16Nb-xTi (x=4,16 wt.%) alloys with mineralized structures was much higher than that on the surface of the untreated alloy after 1 h of culturing (p<0.01). The difference in the number of cells between the untreated and mineralized samples increased even more after 4 h of cultivation. There was also a statistical difference between mineralized Zr-16Nb-4Ti and Zr-16Nb-16Ti alloys, probably due to inconsistencies in the density of the mineralized structure of the selected areas in the two samples, resulting in more MG 63 cells adhering to the surface of the denser Zr-16Nb-16Ti structure. The difference in the number of MG 63 cells on the surface of untreated and mineralized Zr-16Nb-xTi (x=4,16 wt.%) alloys was highest after 24 h, showing that the Zr-16Nb-xTi (x=4,16 wt.%) alloys with mineralized structures promote effective MG 63 cell adhesion (Figure 5n). Cells are more likely to adhere to rougher surfaces than to smooth surfaces [45], and the surface of the mineralized ELR coating had more undulations and grooves and a larger surface area that would be more conducive to cell adhesion. In addition, as the main component of natural bone, HA forms a slightly alkaline environment when degraded, promoting cell adhesion and proliferation [46]. It also provides more binding sites for cells, further promoting cell adhesion to the surfaces of the materials [47].

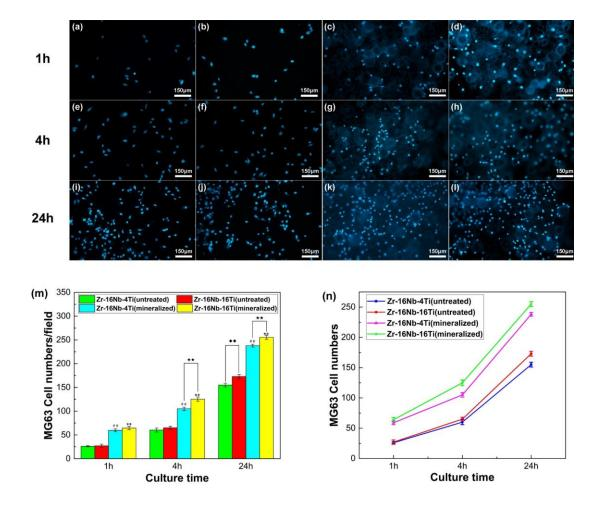
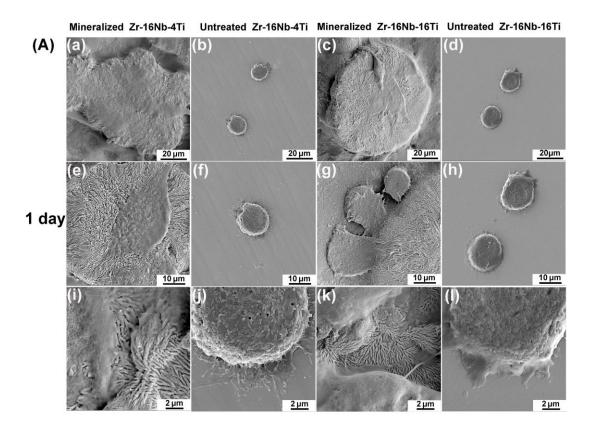


Figure 5. Fluorescence images of MG 63 osteoblast-like cells cultivated on the surface of untreated and mineralized alloys for 1, 4, and 24 h. (a) Untreated Zr-16Nb-4Ti (1 h), (b) Untreated Zr-16Nb-16Ti (1 h), (c) Mineralized Zr-16Nb-4Ti (1 h), (d) Mineralized Zr-16Nb-16Ti (1 h), (e) Untreated Zr-16Nb-4Ti (4 h), (f) Untreated Zr-16Nb-16Ti (4 h), (g) Mineralized Zr-16Nb-4Ti (4 h), (h) Mineralized Zr-16Nb-16Ti (4 h), (i) Untreated Zr-16Nb-4Ti (24 h), (j) Untreated Zr-16Nb-16Ti (24 h), (k) Mineralized Zr-16Nb-4Ti (24 h), (l) Mineralized Zr-16Nb-16Ti (24 h), and (m) Quantitative results of the MG 63 osteoblast-like cells after culturing on untreated and mineralized Zr-16Nb-xTi (x=4,16 wt.%) alloys for 1, 4, and 24 h. # and ## represent p<0.05 and p<0.01, respectively, for untreated Zr-16Nb-4Ti compared with mineralized Zr-16Nb-4Ti. \* and \*\* represent p<0.05 and p<0.01, respectively, for untreated Zr-16Nb-16Ti compared with mineralized Zr-16Nb-16Ti compared with mineralized Zr-16Nb-16Ti compared with mineralized Zr-16Nb-16Ti compared with mineralized Zr-16Nb-16Ti compared with untreated Zr-16Nb-4Ti. (n) Curves of the proliferation of MG 63 cells cultured on untreated and mineralized alloys for 1, 4, and 24 h.

To confirm that the mineralization structures facilitate the adhesion of MG 63 cells, SEM was used to observe MG 63 cells after culturing on untreated and mineralized Zr-16Nb-4Ti and Zr-16Nb-16Ti alloys for 1 day or 3 days. As shown in Figure 6A a, e, i, c, g, and k, MG 63 cells adhered around and inside the mineralized structure after 1 day of culturing and spread easily on the surface of the mineralized structure. Most cells were polygonal and grew lamellipodia because the mineralized structure has a hierarchical multi-level structure that effectively increases the surface contact area compared with the surface of the untreated alloy and is conducive to cell adhesion. Moreover, the mineralization structures have excellent biocompatibility and biological activity, which promote the adhesion and spread of MG 63 cells. In contrast, untreated alloys have smooth surfaces (Figure 6A b, f, j, d, h, and l) with no remarkable microstructures. They lack the ability to promote cell adhesion, making it difficult for cell pseudopodia to grow [48]. The MG 63 cells remained spherical rather than spreading on the surface. Alvaro et al. [29,49] reported that microstructures such as posts, channels, or ravines can facilitate cell adhesion and stimulate cell proliferation. John et al. [50] found similar evidence.

Figure 6B a, e, i, c, g, and k illustrate the morphologies of MG 63 cells adhering to mineralized alloys after 3 days of cultivation. The cells spread more, and more cells were located on or around the mineralized structure. All of the cells had grown lamellipodia and firmly adhered to the mineralized structure. Figure 6B i and k show the connections between MG 63 cells and mineralized structures, implying that these cells prefer to spread on mineralized surfaces. The main component of the mineralized structural coating is fluorine-doped HA. Hydroxyapatite is similar to natural bone in composition and is beneficial for cell spreading [51]. Second, according to Zhou et al. [52], fluorine enhances the ability of the matrix to adsorb OCN and Col-I proteins, further promoting the adhesion and spread of cells to the matrix [53]. Although MG 63 cells spread after 3 days of cultivation, there were fewer lamellipodia around the cells' edges (Figure 6B b, f, j, d, h, and l), indicating weak contact between alloy surfaces and MG 63 cells. Multiple studies have attempted to fabricate various structures at the

micrometer or nanometer levels to increase surface roughness and obtain ravine shapes that enhance substrate biocompatibility and increase bioactivity, eventually improving the relative properties of substrates [24,25,54]. Comparatively, our ELR protein self-assembly technique is more flexible and efficient than traditional surface modification methods.



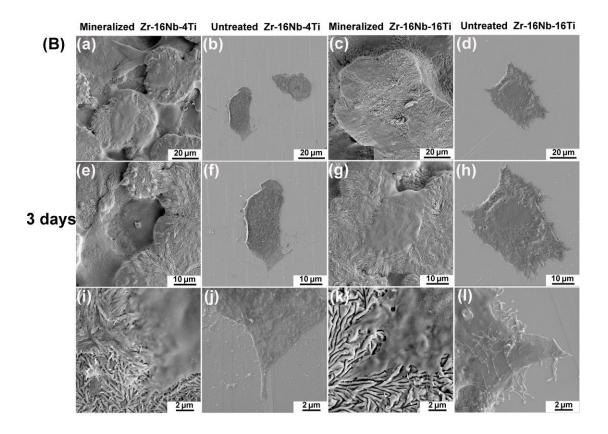


Figure 6. SEM images of MG 63 osteoblast-like cells cultured on mineralized and untreated Zr-16Nb-xTi (x=4,16 wt.%) surfaces for 1 day or 3 days. (A) Mineralized and untreated samples cultured for 1 day. (B) Mineralized and untreated samples cultured for 3 days.

# 3.6.2 Cytocompatibility test

The viability of osteoblast-like MG 63 cells is vital in cytocompatibility. Figure 7a illustrates the relative viability of MG 63 cells cultivated for 1, 3, or 5 days in a medium extracted from untreated and mineralized Zr-16Nb-xTi (x=4,16 wt.%) alloys. The relative viability of MG 63 cells ranged from 101% (untreated Zr-16Nb-4Ti) to 111% (mineralized Zr-16Nb-16Ti) after 1 day of cultivation. Relative cell viability was higher in the experimental groups than in the negative control group, indicating a nontoxic effect. Although the viability of cells in all experimental groups, except the untreated Zr-16Nb-4Ti group, decreased after 3 days of incubation, all samples had higher cell viability than that of the negative control, ranging from 103.1% (untreated Zr-16Nb-16Ti) to 105.1% (mineralized Zr-16Nb-16Ti). Cell viability decreased after 5 days of

cultivation, with the final viability ranging from 95.8% (untreated Zr-16Nb-16Ti) to 103.3% (mineralized Zr-16Nb-16Ti). Based on the cell activity grading system [35], all samples were grade 1 (75%–99%), implying good cytocompatibility. When compared with untreated Zr-16Nb-4Ti and Zr-16Nb-16Ti alloys, the viability of MG 63 cells in mineralized samples remained higher than that of cells in the untreated group during the cultivation period, particularly in the early stages. There was a statistical difference (p<0.01) between the untreated alloy and its corresponding mineralized alloy after 1 day of cultivation. On the third day of culturing, there were statistical differences (p<0.05) between the untreated Zr-16Nb-4Ti, mineralized Zr-16Nb-4Ti, and Zr-16Nb-16Ti and the negative control group. Cell viability in the mineralized samples remained higher (and above 100%) than in the negative control group after 5 days. These results agree with those of previous cell adhesion experiments, indicating that the mineralized samples' biocompatibility was significantly improved. Compared with bioinert materials, HA crystals have no cytotoxicity but have a certain promotional effect on cell proliferation [55]. Furthermore, the mineralized structure generated in this study contained approximately 5.8% fluorine. According to Zhao et al. [56], fluorine promotes the expression of ERK, JNK, and other proteins in cells, improving cell activity and promoting cell proliferation.

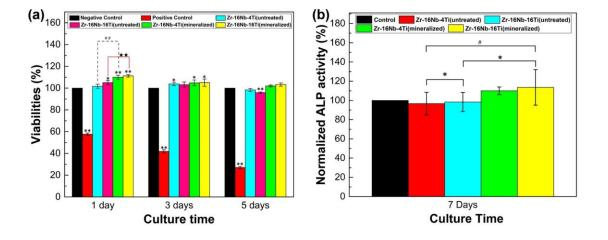


Figure 7. MG 63 cell cytocompatibility test results. (a) Viabilities of MG 63 osteoblast-like cells cultivated for 1, 3, and 5 days in media containing untreated and mineralized Zr-16Nb-xTi (x=4,16 wt.%) alloys. \* and \*\* represent p<0.05 and p<0.01, respectively, compared with the negative

control. # and ## represent p<0.05 and p<0.01, respectively, for untreated Zr-16Nb-4Ti compared with mineralized Zr-16Nb-4Ti. ★ and ★★ represent p<0.05 and p<0.01, respectively, for untreated Zr-16Nb-16Ti compared with mineralized Zr-16Nb-16Ti. (b) Normalized alkaline phosphatase (ALP) activity in MG 63 cell lysates obtained after cultivating cells in extracts of untreated and mineralized Zr-16Nb-xTi (x=4,16 wt.%) alloys for 7 days. \* and # represent p<0.05 and p<0.01, respectively, compared with the different experimental groups.

Alkaline phosphatase is an enzyme secreted by osteoblasts that promotes the mineralization of the extracellular matrix by hydrolyzing phosphates. It is important for evaluating osteoblast differentiation [57]. Normalized ALP activity from untreated and mineralized Zr-16Nb-4Ti and Zr-16Nb-16Ti alloys is shown in Figure 7b. The ALP activity in the untreated group was lower than that in the negative control group. Activity in untreated Zr-16Nb-16Ti (98.36%) was slightly higher than in untreated Zr-16Nb-4Ti (96.66%). Noticeably, ALP activity in mineralized alloy samples improved significantly and showed excellent osteoblast differentiation function, activity in mineralized Zr-16Nb-4Ti (109.98%) and mineralized Zr-16Nb-16Ti (113.59%) confirmed that ELR-mediated mineralization enhanced osteoblast differentiation ability, thereby enhancing the biological activity of the alloys. The differences in the differentiation abilities of osteoblasts are due to the presence of fluorine in the mineralized coating. Studies have shown that fluorapatite stimulates the expression of genes encoding collagen proteins, such as collagen-I, providing a favorable microenvironment for cell proliferation, differentiation, and mineralization, which improve the biological activity of the material [58].

### 3.6.3 Hemolysis rate test

Table 3 illustrates the hemolysis rates of uncoated and mineralized Zr-16Nb-xTi alloys. The hemolysis rates of all test samples were low, indicating negligible effects related to red blood cells. It was also observed that the hemolysis rate of the mineralized sample was higher than that of the uncoated one; however, it is important to note that all samples exhibited a rate of less than 0.5%, which meets the non-hemolytic criteria

Table 3. Hemolysis rates of uncoated and mineralized Zr-16Nb-xTi alloys

Sample	Hemolysis rate (%)	Hemolytic standard	
Uncoated Zr-16Nb-4Ti	0.193(±0.119)	Non-hemolytic	
Uncoated Zr-16Nb-16Ti	0.181(±0.153)	Non-hemolytic	
Mineralized Zr-16Nb-4Ti	0.435(±0.207)	Non-hemolytic	
Mineralized Zr-16Nb-16Ti	0.418(±0.196)	Non-hemolytic	

### 3.6.4 Platelet adhesion test

As shown in Figure 8, the platelet adhesion test revealed differences in the amounts of platelets from uncoated and mineralized alloys. More platelet adhesion was observed on the surface of mineralized Zr-16Nb-xTi, whereas fewer platelets adhered to the uncoated surface. There was no significant difference in platelet adhesion between the uncoated Zr-16Nb-xTi alloys, which is consistent with the hemolysis rate test. The mineralized microstructure's ability to attract platelet adhesion accounts for the higher hemolysis rate of the mineralized alloy. However, no obvious platelet pseudopods were observed on the surfaces of the test samples, and the platelets maintained a regular spherical shape, indicating that all samples had excellent blood compatibility.

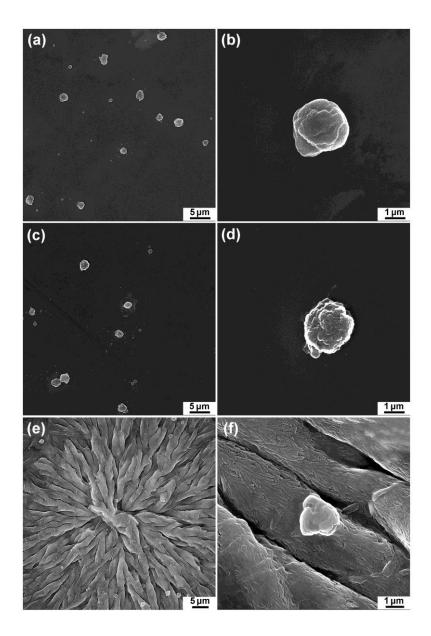


Figure 8. Platelet adhesion on uncoated and mineralized Zr-16Nb-xTi alloys. (a-b) Uncoated Zr-16Nb-4Ti. (c-d) Uncoated Zr-16Nb-16Ti. (e-f) Mineralized Zr-16Nb-xTi alloys.

# 4 Conclusions

This study demonstrates the possibility of improving the biocompatibility of Zr-16Nb-4Ti and Zr-16Nb-16Ti alloys by employing the self-assembly of ELR proteins to fabricate different mineralized structures on the surfaces of Zr-16Nb-xTi (x=4,16 wt.%) alloys. In summary: (1) By adjusting the ELR:HDI ratio to 1:12, we obtained an optimal structure similar to human dental enamel and showed that the large contact area on its

surface promotes cell adhesion and spread. (2) The mineralized structure was nonuniform with regard to its Young's modulus and hardness, as the center area had higher values than the edges, possibly due to differences in densities between the two regions. The mineralized coating was able to maintain high stability under an SBF environment, and it had a relatively high bonding strength with the Zr-16Nb-xTi substrate. (3) Mineralized Zr-16Nb-xTi (x=4,16 wt.%) alloys were shown to have excellent MG 63 cell viability. Unlike the untreated groups, the mineralized samples maintained relatively high viability even after 5 days of culturing. The level of ALP activity demonstrated that the mineralized structure is vital in promoting MG 63 cell differentiation. (4) Cell proliferation assays indicated that MG 63 cells proliferate faster on mineralized surfaces compared with normal Zr-16Nb-xTi (x=4,16 wt.%) alloy surfaces, and subsequent SEM images of the adhesion of MG 63 cells on mineralized surfaces confirmed that the mineralized structure facilitated cell adhesion, promoting the spreading of cells. (5) The hemocompatibility test revealed that mineralized Zr-16Nb-xTi possesses great blood compatibility, and all samples were non-hemolytic. Thus, our study presents a novel approach for improving the biocompatibility of metallic materials, which is more flexible and effective than the traditional surface treatments that are widely used in bone and healing applications. Future work should include research on in vivo biocompatibility to verify the performance of mineralized Zr-16Nb-xTi when used in dental implants and bone regeneration tools.

# 5 Acknowledgments

This work was supported by the National Natural Science Foundation of China (Grant No. 52071339, 51671218), the Natural Science Foundation of Hunan Province, China (Grant No. 2020JJ4739), the ERC Proof-of-Concept Grant (MINGRAFT), and the Medical Research Council (United Kingdom Regenerative Medicine Platform Hub Acellular Smart Materials 3D Architecture, MR/R015651/1).

CRediT authorship contribution statement

Renhao Xue: Investigation, Methodology, Formal analysis, Data curation, Software, Writing – Original Draft. Xinru Deng: Investigation, Formal analysis. Xiaoning Xu: Investigation, Data curation. Yueyan Tian: Investigation. Abshar Hasan: Investigation, Writing – Review & Editing. Alvaro Mata: Supervision, Conceptualization, Writing – Review & Editing. Ligang Zhang: Supervision, Funding acquisition. Libin Liu: Supervision, Validation, Funding acquisition. All authors have read and agreed to the published version of the manuscript.

### 6 References

- [1] M. Kaur, K. Singh, Review on titanium and titanium based alloys as biomaterials for orthopaedic applications, Mater. Sci. Eng. C Mater. Biol. Appl. 102 (2019) 844-862, <a href="https://doi.org/10.1016/j.msec.2019.04.064">https://doi.org/10.1016/j.msec.2019.04.064</a>.
- [2] K. Prasad, O. Bazaka, M. Chua, et al., Metallic biomaterials: current challenges and opportunities, Materials (Basel) 10 (2017) 884, https://doi.org/10.3390/ma10080884.
- [3] J. Davis, Materials for medical devices, ASM handbook Series, (2003).
- [4] J. Park, R.S. Lakes, Biomaterials: an introduction, Springer Science & Business Media, (2007).
- [5] M. Niinomi, M. Nakai, J. Hieda, Development of new metallic alloys for biomedical applications, Acta Biomater. 8 (2012) 3888-3903, <a href="https://doi.org/10.1016/j.actbio.2012.06.037">https://doi.org/10.1016/j.actbio.2012.06.037</a>.
- [6] M.C. Kennady, M.R. Tucker, G.E. Lester, et al., Stress shielding effect of rigid internal fixation plates on mandibular bone grafts. A photon absorption densitometry and quantitative computerized tomographic evaluation, Int. J. Oral Maxillofac. Surg. 18 (1989) 307-310, https://doi.org/10.1016/S0901-5027(89)80101-8.
- [7] R. Huiskes, H. Weinans, B. Van Rietbergen, The relationship between stress shielding and bone resorption around total hip stems and the effects of flexible materials, Clin Orthop Relat Res. 274 (1992) 124-134, <a href="https://doi.org/10.1097/00003086-199201000-00014">https://doi.org/10.1097/00003086-199201000-00014</a>.
- [8] F.M. Bui, K. Bott, M.P. Mintchev, A quantitative study of the pixel-shifting, blurring and nonlinear distortions in MRI images caused by the presence of metal implants, J. Med. Eng. Technol. 24 (2000) 20-27, <a href="https://doi.org/10.1080/030919000294003">https://doi.org/10.1080/030919000294003</a>.
- [9] H. Matsuura, T. Inoue, K. Ogasawara, et al., Quantitative analysis of magnetic

- resonance imaging susceptibility artifacts caused by neurosurgical biomaterials: comparison of 0.5, 1.5, and 3.0 Tesla magnetic fields, Neurol. Med. Chir. (Tokyo) 45 (2005) 395-8; discussion 398, <a href="https://doi.org/10.2176/nmc.45.395">https://doi.org/10.2176/nmc.45.395</a>.
- [10] R. Xue, D. Wang, D. Yang, et al., Novel biocompatible Zr-based alloy with low Young's modulus and magnetic susceptibility for biomedical implants, Materials (Basel) 13 (2020) 5130, <a href="https://doi.org/10.3390/ma13225130">https://doi.org/10.3390/ma13225130</a>.
- [11] X. Zhang, H.A. Awad, R.J. O'Keefe, et al., A perspective: engineering periosteum for structural bone graft healing, Clin. Orthop. Relat. Res. 466 (2008) 1777-1787, https://doi.org/10.1007/s11999-008-0312-6.
- [12] W. Zhou, X. Zhong, X. Wu, et al., The effect of surface roughness and wettability of nanostructured TiO2 film on TCA-8113 epithelial-like cells, Surf. Coat. Technol. 200 (2006) 6155-6160, <a href="https://doi.org/10.1016/j.surfcoat.2005.09.029">https://doi.org/10.1016/j.surfcoat.2005.09.029</a>.
- [13] T. Hryniewicz, R. Rokicki, K. Rokosz, Surface characterization of AISI 316L biomaterials obtained by electropolishing in a magnetic field, Surf. Coat. Technol. 202 (2008) 1668-1673, <a href="https://doi.org/10.1016/j.surfcoat.2007.07.067">https://doi.org/10.1016/j.surfcoat.2007.07.067</a>.
- [14] H.R. Bakhsheshi-Rad, A.F. Ismail, M. Aziz, et al., Co-incorporation of graphene oxide/silver nanoparticle into poly-l-lactic acid fibrous: A route toward the development of cytocompatible and antibacterial coating layer on magnesium implants, Mater. Sci. Eng. C Mater. Biol. Appl. 111 (2020) 110812, <a href="https://doi.org/10.1016/j.msec.2020.110812">https://doi.org/10.1016/j.msec.2020.110812</a>.
- [15] S.N. Saud, R. Hosseinian S, H.R. Bakhsheshi-Rad et al., Corrosion and bioactivity performance of graphene oxide coating on TiNb shape memory alloys in simulated body fluid, Mater. Sci. Eng. C Mater. Biol. Appl. 68 (2016) 687-694, https://doi.org/10.1016/j.msec.2016.06.048.
- [16] S. Parham, A.Z. Kharazi, H.R. Bakhsheshi-Rad, et al., Antimicrobial synthetic and natural polymeric nanofibers as wound dressing: a review, Adv. Eng. Mater. 24 (2022) 2101460, <a href="https://doi.org/10.1002/adem.202101460">https://doi.org/10.1002/adem.202101460</a>.
- [17] A. López-Ortega, V.S. Sáenz de Viteri, S.A. Alves, et al., Multifunctional TiO2 coatings developed by plasma electrolytic oxidation technique on a Ti20Nb20Zr4Ta alloy for dental applications, Biomater. Adv. 138 (2022) 212875, <a href="https://doi.org/10.1016/j.bioadv.2022.212875">https://doi.org/10.1016/j.bioadv.2022.212875</a>.
- [18] R. Tang, C. Shao, L. Chen, et al., A novel CKIP-1 SiRNA slow-release coating on porous titanium implants for enhanced osseointegration, Biomater. Adv. 137 (2022) 212864, <a href="https://doi.org/10.1016/j.bioadv.2022.212864">https://doi.org/10.1016/j.bioadv.2022.212864</a>.
- [19] K. Saravanakumar, M. Abinaya, S. Mehnath, et al., Nano Ag@bioactive microspheres from marine sponge Clathria frondifera: fabrication, fortification, characterization, anticancer and antibacterial potential evaluation, Environ. Res. 206

- (2022) 112282, https://doi.org/10.1016/j.envres.2021.112282.
- [20] J. Qian, W. Zhang, Y. Chen, et al., Osteogenic and angiogenic bioactive collagen entrapped calcium/zinc phosphates coating on biodegradable Zn for orthopedic implant applications, Biomater. Adv. 136 (2022) 212792, <a href="https://doi.org/10.1016/j.bioadv.2022.212792">https://doi.org/10.1016/j.bioadv.2022.212792</a>.
- [21] Y. Zhao, Y. Sun, R. Hang, et al., Biocompatible silane adhesion layer on titanium implants improves angiogenesis and osteogenesis, Biomater. Adv. 139 (2022) 213033, <a href="https://doi.org/10.1016/j.bioadv.2022.213033">https://doi.org/10.1016/j.bioadv.2022.213033</a>.
- [22] S. Mehnath, M. Arjama, M. Rajan, et al., Mineralization of bioactive marine sponge and electrophoretic deposition on Ti-6Al-4V implant for osteointegration, Surf. Coat. Technol. 392 (2020) 125727, <a href="https://doi.org/10.1016/j.surfcoat.2020.125727">https://doi.org/10.1016/j.surfcoat.2020.125727</a>.
- [23] S. Mehnath, M. Jeyaraj, Antibiofilm and enhanced antibiotic delivery by halloysite nanotubes architected dental implant against periodontitis, Mater. Chem. Phys. 295 (2023) 127061, <a href="https://doi.org/10.1016/j.matchemphys.2022.127061">https://doi.org/10.1016/j.matchemphys.2022.127061</a>.
- [24] S.L. Aktug, I. Kutbay, M. Usta, Characterization and formation of bioactive hydroxyapatite coating on commercially pure zirconium by micro arc oxidation, J. Alloys Compd. 695 (2017) 998-1004, https://doi.org/10.1016/j.jallcom.2016.10.217.
- [25] S.L. Aktuğ, S. Durdu, E. Yalçın, et al., Bioactivity and biocompatibility of hydroxyapatite-based bioceramic coatings on zirconium by plasma electrolytic oxidation, Mater. Sci. Eng. C Mater. Biol. Appl. 71 (2017) 1020-1027, https://doi.org/10.1016/j.msec.2016.11.012.
- [26] W. Yao, L. Wu, J. Wang, et al., Micro-arc oxidation of magnesium alloys: a review, J. Mater. Sci. Technol. 118 (2022) 158-180, <a href="https://doi.org/10.1016/j.jmst.2021.11.053">https://doi.org/10.1016/j.jmst.2021.11.053</a>.
- [27] Y. Jeong, B. Moon, H. Choe, et al., Surface characteristics of hydroxyapatite-coated layer prepared on nanotubular Ti–35Ta–xHf alloys by EB-PVD, Thin Solid Films 549 (2013) 147-153, <a href="https://doi.org/10.1016/j.tsf.2013.09.034">https://doi.org/10.1016/j.tsf.2013.09.034</a>.
- [28] J.F. Almine, D.V. Bax, S.M. Mithieux, et al., Elastin-based materials, Chem. Soc. Rev. 39 (2010) 3371-3379, https://doi.org/10.1039/b919452p.
- [29] E. Tejeda-Montes, K.H. Smith, E. Rebollo, et al., Bioactive membranes for bone regeneration applications: effect of physical and biomolecular signals on mesenchymal stem cell behavior, Acta Biomater. 10 (2014) 134-141, <a href="https://doi.org/10.1016/j.actbio.2013.09.001">https://doi.org/10.1016/j.actbio.2013.09.001</a>.
- [30] E. Tejeda-Montes, A. Klymov, M.R. Nejadnik, et al., Mineralization and bone regeneration using a bioactive elastin-like recombinamer membrane, Biomaterials 35 (2014) 8339-8347, https://doi.org/10.1016/j.biomaterials.2014.05.095.

- [31] S. Elsharkawy, M. Al-Jawad, M.F. Pantano, et al., Protein disorder—order interplay to guide the growth of hierarchical mineralized structures, Nat. Commun. 9 (2018) 2145, https://doi.org/10.1038/s41467-018-04319-0.
- [32] X. Deng, A. Hasan, S. Elsharkawy, et al., Topographically guided hierarchical mineralization, Mater. Today Bio 11 (2021) 100119, <a href="https://doi.org/10.1016/j.mtbio.2021.100119">https://doi.org/10.1016/j.mtbio.2021.100119</a>.
- [33] A. Hasan, R. Bagnol, R. Owen, et al., Mineralizing coating on 3D printed scaffolds for the promotion of osseointegration, Front. Bioeng. Biotechnol. 10 (2022) 836386, https://doi.org/10.3389/fbioe.2022.836386.
- [34] W.C. Oliver, G.M. Pharr, An improved technique for determining hardness and elastic modulus using load and displacement sensing indentation experiments, J. Mater. Res. 7 (1992) 1564-1583, <a href="https://doi.org/10.1557/JMR.1992.1564">https://doi.org/10.1557/JMR.1992.1564</a>.
- [35] E. ISO, 10993-12: 2008–Biological evaluation of medical devices–Part 12: Sample preparation and reference materials (ISO 10993-12: 2007).
- [36] F. Y. Zhou, K. J. Qiu, H. F. Li, et al., Screening on binary Zr-1X (X = Ti, Nb, Mo, Cu, Au, Pd, Ag, Ru, Hf and Bi) alloys with good in vitro cytocompatibility and magnetic resonance imaging compatibility, Acta Biomater 9 (2013) 9578-9587, https://doi.org/10.1016/j.actbio.2013.07.035.
- [37] Q. Ruan, J. Moradian-Oldak, Amelogenin and enamel biomimetics, J. Mater. Chem. B 3 (2015) 3112-3129, https://doi.org/10.1039/C5TB00163C.
- [38] S. Bentov, E.D. Aflalo, J. Tynyakov, et al., Calcium phosphate mineralization is widely applied in crustacean mandibles, Sci. Rep. 6 (2016) 22118, <a href="https://doi.org/10.1038/srep22118">https://doi.org/10.1038/srep22118</a>.
- [39] P.K. Zysset, X.E. Guo, C.E. Hoffler, et al., Elastic modulus and hardness of cortical and trabecular bone lamellae measured by nanoindentation in the human femur, J. Biomech. 32 (1999) 1005-1012, <a href="https://doi.org/10.1016/S0021-9290(99)00111-6">https://doi.org/10.1016/S0021-9290(99)00111-6</a>.
- [40] J.H. Kinney, M. Balooch, S.J. Marshall, et al., Atomic force microscope measurements of the hardness and elasticity of peritubular and intertubular human dentin, J. Biomech. Eng. 118 (1996) 133-135, <a href="https://doi.org/10.1115/1.2795939">https://doi.org/10.1115/1.2795939</a>.
- [41] Y. Liu, E.B. Hunziker, N.X. Randall, et al., Proteins incorporated into biomimetically prepared calcium phosphate coatings modulate their mechanical strength and dissolution rate, Biomaterials 24 (2003) 65-70, <a href="https://doi.org/10.1016/S0142-9612(02)00252-1">https://doi.org/10.1016/S0142-9612(02)00252-1</a>.
- [42] N. Ohtsu, T. Takahara, M. Hirano, et al., Effect of treatment temperature on the biocompatibility and mechanical strength of hydroxyapatite coating formed on titanium using calcium phosphate slurry, Surf. Coat. Technol. 239 (2014) 185-190,

### http://doi.org/10.1016/j.surfcoat.2013.11.038.

- [43] L. Bai, Y. Liu, Z. Du, et al., Differential effect of hydroxyapatite nano-particle versus nano-rod decorated titanium micro-surface on osseointegration, Acta Biomater. 76 (2018) 344-358, <a href="https://doi.org/10.1016/j.actbio.2018.06.023">https://doi.org/10.1016/j.actbio.2018.06.023</a>.
- [44] Q. Du, D. Wei, S. Cheng, et al., Rapid structural evolution and bone inducing mechanism of the multilayer coating with silicon-doped hydroxyapatite crystals on the microwave water steaming-hydrothermally treated titania coating, Appl. Surf. Sci. 539 (2021) 148153, https://doi.org/10.1016/j.apsusc.2020.148153.
- [45] L. Ramaglia, G. Di Spigna, G. Capece, et al., Differentiation, apoptosis, and GM-CSF receptor expression of human gingival fibroblasts on a titanium surface treated by a dual acid-etched procedure, Clin. Oral Investig. 19 (2015) 2245-2253, <a href="https://doi.org/10.1007/s00784-015-1469-5">https://doi.org/10.1007/s00784-015-1469-5</a>.
- [46] C. Gao, Y. Deng, P. Feng, et al., Current progress in bioactive ceramic scaffolds for bone repair and regeneration, Int. J. Mol. Sci. 15 (2014) 4714-4732, https://doi.org/10.3390/ijms15034714.
- [47] C. Liao, J. Zhou, Replica-exchange molecular dynamics simulation of basic fibroblast growth factor adsorption on hydroxyapatite, J. Phys. Chem. B 118 (2014) 5843-5852, <a href="https://doi.org/10.1021/jp501463r">https://doi.org/10.1021/jp501463r</a>.
- [48] Q.M. Zhao, X.K. Li, S. Guo, et al., Osteogenic activity of a titanium surface modified with silicon-doped titanium dioxide, Mater. Sci. Eng. C Mater. Biol. Appl. 110 (2020) 110682, <a href="https://doi.org/10.1016/j.msec.2020.110682">https://doi.org/10.1016/j.msec.2020.110682</a>.
- [49] A. Mata, C. Boehm, A.J. Fleischman, et al., Connective tissue progenitor cell growth characteristics on textured substrates, Int. J. Nanomedicine 2 (2007) 389-406.
- [50] J.L. Tan, J. Tien, D.M. Pirone, et al., Cells lying on a bed of microneedles: an approach to isolate mechanical force, Proc. Natl. Acad. Sci. U. S. A. 100 (2003) 1484-1489, https://doi.org/10.1073/pnas.0235407100.
- [51] M. Lu, H. Chen, B. Yuan, et al., Electrochemical deposition of nanostructured hydroxyapatite coating on titanium with enhanced early stage osteogenic activity and osseointegration, Int. J. Nanomedicine 15 (2020) 6605-6618, <a href="https://doi.org/10.2147/IJN.S268372">https://doi.org/10.2147/IJN.S268372</a>.
- [52] J. Zhou, B. Li, Y. Han, F-doped TiO2 microporous coating on titanium with enhanced antibacterial and osteogenic activities, Sci. Rep. 8 (2018) 17858, <a href="https://doi.org/10.1038/s41598-018-35875-6">https://doi.org/10.1038/s41598-018-35875-6</a>.
- [53] J. Zhou, B. Li, L. Zhao, et al., F-doped micropore/nanorod hierarchically patterned coatings for improving antibacterial and osteogenic activities of bone implants in bacteria-infected cases, ACS Biomater. Sci. Eng. 3 (2017) 1437-1450,

#### https://doi.org/10.1021/acsbiomaterials.6b00710.

- [54] M.R. Steedman, S.L. Tao, H. Klassen, et al., Enhanced differentiation of retinal progenitor cells using microfabricated topographical cues, Biomed. Microdevices 12 (2010) 363-369, <a href="https://doi.org/10.1007/s10544-009-9392-7">https://doi.org/10.1007/s10544-009-9392-7</a>.
- [55] Q. Du, D. Wei, S. Wang, et al., Rapidly formation of the highly bioactive surface with hydroxyapatite crystals on the titania micro arc oxidation coating by microwave hydrothermal treatment, Appl. Surf. Sci. 487 (2019) 708-718, <a href="https://doi.org/10.1016/j.apsusc.2019.05.165">https://doi.org/10.1016/j.apsusc.2019.05.165</a>.
- [56] Q. Zhao, L. Yi, A. Hu, et al., Antibacterial and osteogenic activity of a multifunctional microporous coating codoped with Mg, Cu and F on titanium, J. Mater. Chem. B 7 (2019) 2284-2299, <a href="https://doi.org/10.1039/C8TB03377C">https://doi.org/10.1039/C8TB03377C</a>.
- [57] Q. Zhao, G. Xu, A. Hu, et al., A Mg/Zn-co-doped composite coating on a titanium surface enhances osteogenic activity through the Wnt/β-catenin pathway, Appl. Surf. Sci. 515 (2020) 146072, <a href="https://doi.org/10.1016/j.apsusc.2020.146072">https://doi.org/10.1016/j.apsusc.2020.146072</a>.
- [58] X. Wang, T. Jin, S. Chang, et al., In vitro differentiation and mineralization of dental pulp stem cells on enamel-like fluorapatite surfaces, Tissue Eng. Part C Methods 18 (2012) 821-830, <a href="https://doi.org/10.1089/ten.TEC.2011.0624">https://doi.org/10.1089/ten.TEC.2011.0624</a>.
- [59] ASTM-F756-00, Standard practice for assessment of hemolytic properties of materials, in: Annual book of Astm standards, American Society for Testing and Materials, Philadelphia, PA, USA, (2000).